Research Article | Vol. 25, No. 23 | 13 Nov 2017 | OPTICS EXPRESS 29216

Optics EXPRESS

Wavelength scaling of the cutoff energy in the solid high harmonic generation

XI LIU,[1] XIAOSONG ZHU,[1,*] XIAOFAN ZHANG,[1] DIAN WANG,[1] PENGFEI LAN [1] AND PEIXIANG LU[1,2,3]

[1] *Wuhan National Laboratory for Optoelectronics and School of Physics, Huazhong University of Science and Technology, Wuhan 430074, China*
[2] *Laboratory of Optical Information Technology, Wuhan Institute of Technology, Wuhan 430205, China*
[3] *lupeixiang@mail.hust.edu.cn*
[*] *zhuxiaosong@hust.edu.cn*

Abstract: The wavelength scaling of the cutoff energy in solid high harmonic generation (HHG) is investigated theoretically by separating the contributions into the intraband and interband components. We find that, the cutoff energies of intraband and interband HHG exhibit the essentially different wavelength dependences. Specifically, the cutoff energy of the intraband HHG is wavelength independent, whereas the cutoff energy of the interband HHG depends linearly on the laser wavelength. Our results can uniformly interpret two current different wavelength scalings of the cutoff energy reported in previous researches. The fundamentally different wavelength scalings of the cutoff energy for intraband and interband HHG can be used to distinguish the two mechanisms.

OCIS codes: (270.6620) Strong-field processes; (190.4160) Multiharmonic generation; (190.4720) Optical nonlinearities of condensed matter.

References and links

1. F. Krausz, and M. Ivanov, "Attosecond physics," Rev. Mod. Phys. **81**, 163–234 (2009).
2. P. B. Corkum, and F. Krausz, "Attosecond science," Nat. Phys. **3**, 381–387 (2007).
3. X. Ma, M. Li, Y. Zhou, and P. Lu, "Nonsequential double ionization of Xe by mid-infrared laser pulses," Opt. Quantum Electron. **49**, 170 (2017).
4. Y. Zhou, M. Li, Y. Li, A. Tong, Q. Li, and P. Lu, "Dissection of electron correlation in strong-field sequential double ionization using a classical model," Opt. Express **25**, 8450–8458 (2017).
5. P. B. Corkum, "Plasma perspective on strong-field multiphoton ionization," Phys. Rev. Lett. **71**, 1994–1997 (1993).
6. M. Lewenstein, P. Balcou, M. Y. Ivanov, A. L'Huillier, and P. B. Corkum, "Theory of hihg-harmonic generation by low-frequency laser fields," Phys. Rev. A **49**, 2117–2132 (1994).
7. M. Hentschel, R. Kienberger, C. Spielmann, G. A. Reider, N. Milosevic, T. Brabec, P. Corkum, U. Heinzmann, M. Drescher, and F. Krausz, "Attosecond metrology," Nature **414**, 509–513 (2001).
8. P. M. Paul, E. S. Toma, P. Breger, G. Mullot, F. Augé, P. Balcou, H. G. Muller, and P. Agostini, "Observation of a Train of Attosecond Pulses from High Harmonic Generation," Science **292**, 1689–1692 (2005).
9. L. Li, Z. Wang, F. Li, and H. Long, "Efficient generation of highly elliptically polarized attosecond pulses," Opt. Quantum Electron. **49**, 73 (2017).
10. C. Yu, H. He, Y. Wang, Q. Shi, Y. Zhang, and R. Lu, "Intense attosecond pulse generated from a molecular harmonic plateau of H_2^+ in mid-infrared laser fields," J. Phys. B: At. Mol. Opt. Phys. **47**, 055601 (2014).
11. J. Itatani, J. Levesque, D. Zeidler, H. Niikura, H. Pépin, J. C. Kieffer, P. B. Corkum, and D. M. Villeneuve, "Tomographic imaging of molecular orbitals," Nature **432**, 867–871 (2004).
12. S. Haessler, J. Caillat, W. Boutu, C. Giovanetti-Teixeira, T. Ruchon, T. Auguste, Z. Diveki, P. Breger, A. Maquet, B. Carré, R. Taïeb, and P. Salières, "Attosecond imaging of molecular electronic wavepackets," Nat. Phys. **6**, 200–206 (2010).
13. C. Zhai, X. Zhu, P. Lan, F. Wang, L. He, W. Shi, Y. Li, M. Li, Q. Zhang, and P. Lu, "Diffractive molecular-orbital tomography," Phys. Rev. A **95**, 033420 (2017).
14. X. Liu, P. Li, X. Zhu, P. Lan, Q. Zhang, and P. Lu, "Probing the $\pi - \pi^*$ transitions in conjugated compounds with an infrared femtosecond laser," Phys. Rev. A **95**, 033421 (2017).
15. P. Lan, M. Ruhmann, L. He, C. Zhai, F. Wang, X. Zhu, Q. Zhang, Y. Zhou, M. Li, M. Lein, and P. Lu, "Attosecond Probing of Nuclear Dynamics with Trajectory–Resolved High–Harmonic Spectroscopy," Phys. Rev. Lett. **119**, 033201 (2017).

#308402 https://doi.org/10.1364/OE/25.029216
Journal © 2017 Received 2 Oct 2017; revised 1 Nov 2017; accepted 2 Nov 2017; published 8 Nov 2017

Optics EXPRESS

16. S. Ghimire, A. D. DiChiara, E. Sistrunk, P. Agostini, L. F. DiMauro, and D. A. Reis, "Observation of high-order harmonic generation in a bulk crystal," Nat. Phys. **7**, 138–141 (2011).
17. T. T. Luu, M. Garg, S. Y. Kruchinin, A. Moulet, M. T. Hassan, and E. Goulielmakis, "Extreme ultraviolet high-harmonic spectroscopy of solids," Nature **521**, 498–502 (2015).
18. H. Long, L. Bao, A. A. Habeeb, and P. Lu, "Effects of doping concentration on the surface plasmonic resonances and optical nonlinearities in AGZO nanotriangle arrays," Opt. Quantum Electron. **49**, 345 (2017).
19. G. Vampa, T. J. Hammond, N. Thiré, B. E. Schmidt, F. Légaré, C. R. McDonald, T. Brabec, D. D. Klug, and P. B. Corkum, "All-Optical Reconstruction of Crystal Band Structure," Phys. Rev. Lett. **115**, 193603 (2015).
20. A. A. Lanin, E. A. Stepanov, A. B. Fedotov, and A. M. Zheltikov, "Mapping the electron band structure by intraband high-harmonic generation in solids," Optica **4**, 516–519 (2017).
21. C. M. Wang, T. S. Ho, and S. I. Chu, "Determination of band structure from the intra-band power spectrum of high harmonic generation in crystal," J. Phys. B: At. Mol. Opt. Phys. **49**, 225401 (2016).
22. M. Schultze, K. Ramasesha, C. D. Pemmaraju, S. A. Sato, D. Whitmore, A. Gandman, J. S. Prell, L. J. Borja, D. Prendergast, K. Yabana, D. M. Neumark, and S. R. Leone, "Attosecond band-gap dynamics in silicon," Science **346**, 1348–1352 (2014).
23. M. Hohenleutner, F. Langer, O. Schubert, M. Knorr, U. Huttner, S. W. Koch, M. Kira, and R. Huber, "Real-time observation of interfering crystal electrons in high-harmonic generation," Nature **523**, 572–575 (2015).
24. S. Jiang, C. Yu, G. Yuan, T. Wu, Z. Wang, and R. Lu, "Quantum–trajectory analysis for charge transfer in solid materials induced by strong laser felds," J. Phys.: Condens. Matter **29**, 275702 (2017).
25. T. Higuchi, M. I. Stockman, and P. Hommelhoff, "Strong-Field Perspective on High-Harmonic Radiation from Bulk Solids," Phys. Rev. Lett. **113**, 213901 (2014).
26. S. Ghimire, A. D. DiChiara, E. Sistrunk, G. Ndabashimiye, U. B. Szafruga, A. Mohammad, P. Agostini, L. F. DiMauro, and D. A. Reis, "Generation and propagation of high-order harmonics in crystals," Phys. Rev. A **85**, 043836 (2012).
27. S. Ghimire, G. Ndabashimiye, A. D. DiChiara, E. Sistrunk, M. I. Stockman, P. Agostini, L. F. DiMauro, and D. A. Reis, "Strong-field and attosecond physics in solids," J. Phys. B: At. Mol. Opt. Phys. **47**, 204030 (2014).
28. E. N. Osika, A. Chacón, L. Ortmann, N. Suárez, J. A. Pérez-Hernández, B. Szafran, M. F. Ciappina, F. Sols, A. S. Landsman, and M. Lewenstein, "Wannier-Bloch Approach to Localization in High-Harmonics Generation in Solids," Phys. Rev. X **7**, 021017 (2017).
29. G. Vampa, C. R. McDonald, G. Orlando, P. B. Corkum, and T. Brabec, "Semiclassical analysis of high harmonic generation in bulk crystals," Phys. Rev. B **91**, 064302 (2015).
30. Z. Guan, X. X. Zhou, and X. B. Bian, "High-order-harmonic generation from periodic potentials driven by few-cycle laser pulses," Phys. Rev. A **93**, 033852 (2016).
31. M. Wu, S. Ghimire, D. A. Reis, K. J. Schafer, and M. B. Gaarde, "High-harmonic generation from Bloch electrons in solids," Phys. Rev. A **91**, 043839 (2015).
32. M. Wu, D. A. Browne, K. J. Schafer, and M. B. Gaarde, "Multilevel perspective on high-order harmonic generation in solids," Phys. Rev. A **94**, 063403 (2016).
33. L. A. Chizhova, F. Libisch, and J. Burgdörfer, "High-harmonic generation in graphene: Interband response and the harmonic cutoff," Phys. Rev. B **95**, 085436 (2017).
34. N. Tancogne-Dejean, O. D. Mücke, F. X. Kärtner, and A. Rubio, "Impact of the Electronic Band Structure in High-Harmonic Generation Spectra of Solids," Phys. Rev. Lett. **118**, 087403 (2017).
35. J. C. Slater, "A Soluble Problem in Energy Bands," Phys. Rev. **87**, 808 (1952).
36. T. Y. Du, Z. Guan, X. X. Zhou, and X. B. Bian, "Enhanced high-order harmonic generation from periodic potentials in inhomogeneous laser fields," Phys. Rev. A **94**, 023419 (2016).
37. X. Liu, X. Zhu, P. Lan, X. Zhang, D. Wang, Q. Zhang, and P. Lu, "Time-dependent population imaging for high-order-harmonic generation in solids," Phys. Rev. A **95**, 063419 (2017).
38. J. B. Li, X. Zhang, S. J. Yue, H. M. Wu, B. T. Hu, and H. C. Du, "Enhancement of the second plateau in solid high-order harmonic spectra by the two-color fields," Opt. Express **25**, 18603–18613 (2017).
39. T. Huang, X. Zhu, L. Li, X. Liu, P. Lan, and P. Lu, "High–order harmonic generation of doped semiconductor," Phys. Rev. A **96**, 043425 (2017).
40. T. Ikemachi, Y. Shinohara, T. Sato, J. Yumoto, M. Kuwata-Gonokami, and K. L. Ishikawa, "Trajectory analysis of high–order–harmonic generation from periodic crystals," Phys. Rev. A **95**, 043416 (2017).
41. M. D. Feit, J. A. Fleck, Jr., and A. Steiger, "Solution of the Schrödinger equation by a spectral method," J. Comput. Phys. **47**, 412–433 (1982).
42. G. Vampa, C. R. McDonald, G. Orlando, D. D. Klug, P. B. Corkum, and T. Brabec, "Theoretical Analysis of High-Harmonic Generation in Solids," Phys. Rev. Lett. **113**, 073901 (2014).
43. C. R. McDonald, G. Vampa, P. B. Corkum, and T. Brabec, "Interband Bloch oscillation mechanism for high-harmonic generation in semiconductor crystals," Phys. Rev. A **92**, 033845 (2015).
44. C. Yu, X. Zhang, S. Jiang, X. Cao, G. Yuan, T. Wu, L. Bai, and R. Lu, "Dependence of high–order–harmonic generation on dipole moment in SiO2 crystals," Phys. Rev. A **94**, 013846 (2016).
45. C. Liu, Y. Zheng, Z. Zeng, and R. Li, "Effect of elliptical polarization of driving field on high–order–harmonic generation in semiconductor ZnO," Phys. Rev. A **93**, 043806 (2016).
46. U. Elu, M. Baudisch, H. Pires, F. Tani, M. H. Frosz, F. Köttig, A. Ermolov, P. ST.J. Russell, and J. Biegert, "High average power and single–cycle pulses from a mid–IR optical parametric chirped pulse amplifier," Optica **4**,

Optics EXPRESS

1024–1029 (2017).
47. S. A. Rezvani, Z. Hong, X. Pang, S. Wu, Q. Zhang, and P. Lu, "Ultrabroadband tunable OPA design using a spectrally broadened pump source," Opt. Lett. **42**, 3367-3370 (2017).
48. O. Schubert, M. Hohenleutner, F. Langer, B. Urbanek, C. Lange, U. Huttner, D. Golde, T. Meier, M. Kira, S. W. Koch, and R. Huber, "Sub-cycle control of terahertz high-harmonic generation by dynamical Bloch oscillations," Nat. Photonics **8**, 119–123 (2014).

1. Introduction

The interaction of intense laser pulses with atomic and molecular gases has uncovered many interesting strong field phenomena in the past several decades [1–4]. High harmonic generation (HHG) is one of the most fascinating processes among these phenomena [5, 6]. As an ultrafast nonlinear process, HHG in gases nowadays is generally used to produce coherent extreme ultraviolet (XUV) attosecond pulses [7–10] and probe electronic structures or dynamics of atomic or molecular targets [11–15]. Recently, the experimental observations [16] of HHG from bulk crystals have extended the target materials from gases to solids, which opens up a novel field of studying the attosecond electron dynamics in condensed matter. Compared with gas HHG, the solid HHG has the potential superiority to obtain the compact and brighter XUV light source due to the higher electronic density of crystals [17, 18]. Besides, the solid HHG also provides an effective way to achieve the all-optical reconstruction of the energy–band structure [19–21] and even to control the ultrafast electron dynamics in solids [17, 22–24].

A harmonic spectrum is typically composed of a rapid decline at first several orders followed by a plateau and a sharp cutoff. For the gas HHG, the cutoff energy is well predicted as $I_p + 3.17U_p$ by the semiclassical three-step model [5], where I_p is the ionization potential and U_p is the ponderomotive energy. U_p is associated with the amplitude F_0 and angular frequency ω of the laser field, and is expressed as $U_p = F_0^2/4\omega^2$. This suggests that the cutoff energy of gas HHG is proportional to the square of both the field strength and wavelength of the laser pulse. For the solid HHG, it has been widely accepted that the cutoff energy exhibits a linear dependence on field strength F_0 [16, 17, 25–33]. However, the wavelength dependence of the cutoff energy in solid HHG is still controversial at present. Some studies claimed that the cutoff energy of the solid HHG is wavelength independent [25–28, 34], whereas others found it depends linearly on the wavelength [29–33].

In this work, we investigate the wavelength scaling of the cutoff energy for the solid HHG by distinguishing the contributions from the intraband and interband channels. It is found that the cutoff energy of the intraband HHG is independent of the laser wavelength. Nevertheless, the cutoff energy of the interband HHG is linearly dependent on the laser wavelength. For the overall (intraband + interband) HHG, the wavelength scaling of the cutoff energy is determined by which mechanism (intraband or interband) is dominant in the cutoff region. For example, the cutoff energy of the observed harmonics will increase linearly with the laser wavelength if the interband HHG is dominant in the cutoff region. Our result clarifies the controversy of two present different wavelength dependences of the cutoff energy, revealing that the discrepancy originates from two different HHG mechanisms. We also further verify the field strength dependence of the cutoff energy via the intraband and interband channels, and find that the cutoff energies of both intraband and interband HHG increase linearly with the field strength. Thus the cutoff energy of overall HHG always shows a linear dependence on the field strength, which is in good agreement with the previous consensus in research community. The fundamentally different wavelength scalings of the cutoff energy for intraband and interband HHG provide a useful tool to distinguish the two mechanisms.

Optics EXPRESS

2. Theoretical model

In our simulation, the laser-solid interaction is described with a one–dimensional single–active electron model. The field–free Hamiltonian $\hat{H}_0$ is written as (atomic units are used throughout this paper unless otherwise stated) $\hat{H}_0 = \hat{p}^2/2 + V(x)$, where $\hat{p}$ is the momentum operator and $V(x)$ is the periodic lattice potential. In the model, we adopt the Mathieu-type potential $V(x) = -V_0[1 + \cos(2\pi x/a_0)]$, with $V_0 = 0.37$ a.u. and lattice constant $a_0 = 8$ a.u. The Mathieu-type potential [35] is a typical periodic potential and has been widely used for the previous solid HHG studies [30–32, 36–40]. In this work, our calculation is based on a finite but long enough cell chain with 60 lattice periods, i.e., the space region of the simulation box is [-240, 240] a.u. The finiteness of the coordinate space in our model requires that an absorbing boundary needs to be added to avoid the reflection from the edges of the simulation box when the time-dependent evolution is performed as in the gas HHG simulation. The energy–band structure of the model can be given by solving the eigen equation of $\hat{H}_0$, namely

$$\hat{H}_0\phi_n(x) = E_n\phi_n(x), \tag{1}$$

where n is the eigenstate number. E_n and $\phi_n(x)$ are the corresponding eigenenergy and eigenstate wavefunction, respectively. Equation (1) is numerically solved by the diagonalization scheme in the coordinate grid. Specifically, E_n and $\phi_n(x)$ are obtained by solving the eigenvalues and eigenvector of matrix $\mathbf{H}$, respectively. $\mathbf{H}$ is a symmetric banded matrix, whose nonzero elements are given by

$$\begin{aligned} \mathbf{H}_{i,i} &= \frac{1}{(\Delta x)^2} + V_i, \\ \mathbf{H}_{i,i+1} &= -\frac{1}{2(\Delta x)^2}, \\ \mathbf{H}_{i+1,i} &= \mathbf{H}_{i,i+1}, \end{aligned} \tag{2}$$

where Δx is the grid spacing and V_i is the ith element of the one-dimensional grid of $V(x)$. The obtained band structures are shown in the Fig. 1(a). In contrast, we also calculate the band structures in the reciprocal space by the Bloch-state expansion as shown in the Fig. 1(b). One can see that the resulting band structures obtained by two methods are in good agreement. In Figs. 1(a) and 1(b), only the valence band VB and the first conduction band CB are presented. The primary plateau is contributed mainly by the VB and CB, whereas the latter plateaus are involved with higher-lying conduction bands [30–32, 37]. In our calculation, the second plateau can also be observed in the harmonic spectrum. However, we will focus only on the primary plateau of the harmonic spectrum considering that the higher plateaus are much weaker.

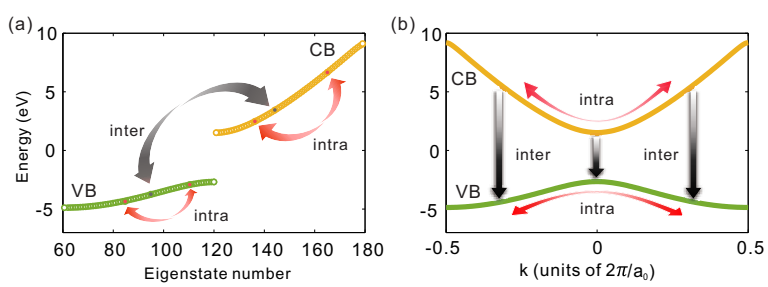

Fig. 1. The band structures calculated by the (a) diagonalization scheme in coordinate space and (b) Bloch-state expansion in reciprocal space. The red and black arrows indicate the intraband and interband dynamics, respectively.

Optics EXPRESS

The evolution of the solid system in the laser field is simulated by solving the time-dependent Schrödinger equation (TDSE). In the length gauge, the time-dependent Hamiltonian is written as

$$\hat{H}(t) = \hat{H}_0 + xF(t), \tag{3}$$

where $F(t)$ is the electric field. The dipole approximation is adopted since the wavelengths used in this work are much larger than the lattice constant. The time-dependent wavefunction $\psi(t)$ is propagated over time using the split-operator technique [41]. In our model, only a small portion of electrons populated near $k = 0$ in VB can tunnel into conduction bands under the laser parameters used in current works. Therefore, just as the treatment in [30, 32, 36–39], we choose the eigenstate with $k = 0$ in VB as the initial state. A more detailed discussion about it can be referred to in [37]. The width of the absorbing boundary is 40 a.u. in our calculation. The sine-squared envelope is adopted for all laser pulses in this paper. After obtaining $\psi(t)$ at each time step, the laser–induced current is calculated by

$$j(t) = -\langle \psi(t) \mid \hat{p} \mid \psi(t) \rangle . \tag{4}$$

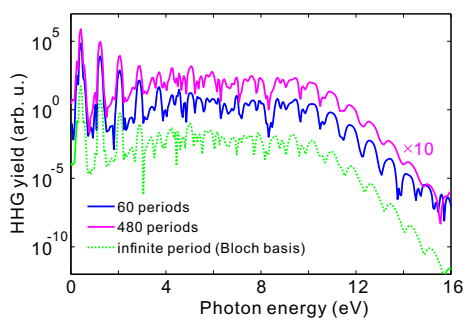

Fig. 2. High harmonic spectra contributed by overall currents from the cell chains of 60 periods, 480 periods and the infinite period. The laser wavelength is 3.00 μm and the laser intensity is 6.00×10^{11} W/cm^2. The duration is 8 optical cycles for all laser pulses.

It has been widely recognized that the HHG in solids originates from two distinct contributions: the intraband current and interband current [31, 42–45]. As shown in Figs. 1(a) and 1(b), the intraband current arises from the laser–driven Bloch oscillations of electrons in individual bands, whereas the interband current involves with the electron transitions between the valence and conduction bands. The significant advantage of our theoretical approach is that the intraband and interband currents can be separated easily in the model. Specifically, the time-dependence wavefunction $\psi(t)$ is expanded as

$$|\psi(t)\rangle = \sum_b \sum_i c_i^b(t) \left|\phi_i^b\right\rangle, \tag{5}$$

where b is the band index and i is the state index for the corresponding band b. By inserting Eq.(5) into Eq.(4), the intraband current j_{intra} and interband current j_{inter} can be written as [30]

$$j_{\text{intra}}(t) = -\sum_b \sum_{ii'} c_i^{b*} c_{i'}^b \left\langle \phi_i^b \mid \hat{p} \mid \phi_{i'}^b \right\rangle, \tag{6}$$

$$j_{\text{inter}}(t) = -\sum_{\substack{bb' \\ b \neq b'}} \sum_{ii'} c_i^{b*} c_{i'}^{b'} \left\langle \phi_i^b \mid \hat{p} \mid \phi_{i'}^{b'} \right\rangle, \tag{7}$$

Optics EXPRESS

respectively. The total laser–induced current $j(t)$ satisfies

$$j(t) = j_{\text{intra}}(t) + j_{\text{inter}}(t). \tag{8}$$

The high harmonic spectra contributed by the intraband and/or interband channels are obtained by the Fourier transform of the corresponding laser-induced current.

In order to demonstrate the validity of our theoretical model, the overall harmonic spectra calculated by the cell chains of 60 periods, 480 periods and the infinite cell chain are shown in Fig. 2. Herein, the infinite cell chain is modeled by the periodic boundary condition (PBC) in velocity gauge based on the Bloch basis [40]. The laser wavelength is 3.00 μm and the laser intensity is 6.00×10^{11} W/cm^2. As shown in Fig. 2, one can see that the profiles of the harmonic spectra obtained by the three models are very close to each other. This consistency confirms that our numerical model is convergent and valid for the solid HHG simulation.

3. Results and discussions

In order to study the wavelength scaling of the cutoff energy for the solid HHG, we first investigate the harmonic spectra contributed from the intraband, interband and overall currents by varying the laser wavelength in the mid-infrared (MIR) region [46, 47] with a constant field strength. The laser wavelength ranges from 1.50 μm to 3.60 μm, and the laser intensity is 6.00×10^{11} W/cm^2. The total duration of the laser pulse is 8 optical cycles. The bandgap of VB and CB in our model is $\Delta E = 4.20$ eV.

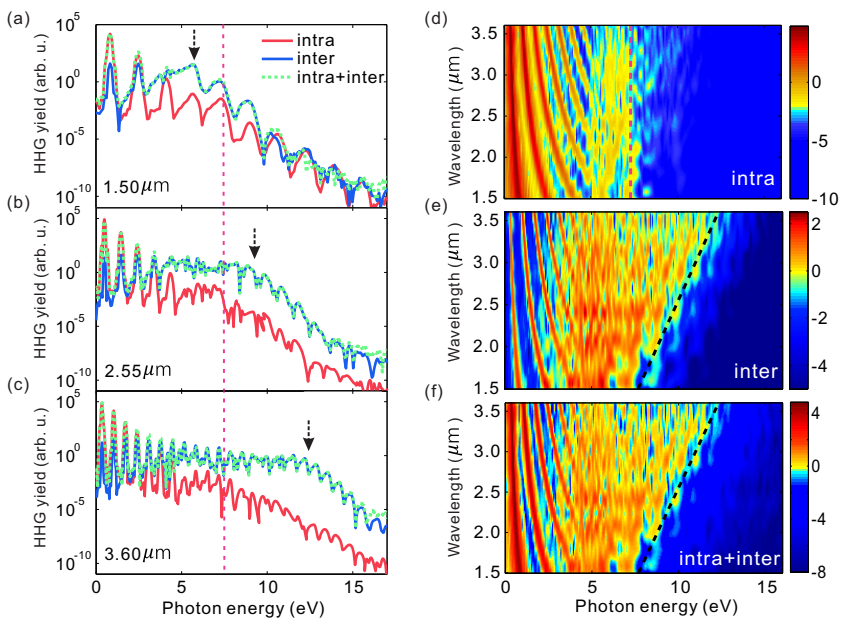

Fig. 3. High harmonic spectra contributed by intraband, interband and overall currents with wavelength (a) 1.50 μm, (b) 2.55 μm and (c) 3.60 μm, respectively. High harmonic spectra (with a logarithmic color scale) contributed by (d) intraband, (e) interband and (f) overall currents with the laser wavelength varying from 1.50 μm to 3.60 μm, respectively. The vertical pink lines in panels (a)–(d) indicate the position of photon energy 7.30 eV. The black arrows in panels (a)–(c) and the dashed black lines in panels (e) and (f) indicate the cutoff of the interband HHG. The laser intensity is 6.00×10^{11} W/cm^2 and the duration is 8 optical cycles for all laser pulses.

The obtained harmonic spectra with laser wavelength $\lambda = 1.50$ μm, 2.55 μm and 3.60 μm

Optics EXPRESS

are shown in Figs. 3(a)–3(c), respectively. One can see clearly that the intraband contribution is dominant for the harmonics with photon energy low than the bandgap ΔE, whereas the interband response dominates the harmonics in the plateau and cutoff regions. The wavelength dependences of the cutoff energy for the intraband and interband HHG are prominently different. Throughout the paper, the cutoff in a harmonic spectrum is judged according to the position where the harmonic efficiency decreases dramatically after a primary plateau. As indicated by the dashed pink vertical line in Figs. 3(a)–3(c), the cutoffs of the intraband HHG always locate at about the position of 7.30 eV. However, for the interband HHG, as indicated by the black arrows, the cutoff energies for laser wavelengths 1.50 μm, 2.55 μm and 3.60 μm are 5.69 eV, 8.94 eV and 12.19 eV, respectively. This trend of monotonous increase shows that the cutoff energy of interband HHG is wavelength sensitive. Figures 3(d)–3(f) show the harmonic spectra calculated by intraband, interband and overall currents, respectively. The wavelength step is 0.15 μm. In Fig. 3(d), it can be seen that the cutoff energies for all wavelengths are concentrated near 7.30 eV. This result further confirms that the cutoff energy of intraband HHG is independent of the laser wavelength. In contrast, as indicated by the dashed black line in Fig. 3 (e), the cutoff energy of the interband HHG shows a linear dependence on the wavelength. Considering that the interband HHG is dominant in the cutoff region within the current laser parameters, the cutoff energy of the overall HHG should be identical to that of the interband HHG. Thus, the cutoff energy of overall HHG also depends linearly on the wavelength as shown in Fig. 3 (f). The similar linear wavelength scalings of the cutoff energy claimed in [29–33] are actually due to the fact that the interband mechanism is dominant in their works. In these works, the coupling between valence and conduction is similar to a two–level system, where the coupling strength is proportional to the potential vector of the laser field. The cutoff energy of the interband HHG caused by the interband transition is limited to the energy difference between the valence and conduction bands.

In the above discussion, HHG is dominantly contributed by the interband component. In order to discuss the case that the intraband HHG dominates the observed harmonic spectra, we extend the laser wavelength into the terahertz region. When the wavelength is long enough, the electrons in valence band can hardly tunnel into conduction bands and are particularly inclined to oscillating periodically in respective bands. Therefore, the intraband mechanism can govern the overall HHG in the terahertz regime [29, 43, 48]. Figure 4(a) shows the harmonic spectra from intraband, interband and overall currents with laser wavelength 40.00 μm. The total duration of the laser pulse is 2 optical cycles, and the laser intensity is 1.00×10^{10} W/cm^2. One can see that the intraband process dominates the harmonic radiations spanning the entire harmonic spectra. The harmonic spectrum contributed by the overall current is identical to the component contributed by the intraband current. Thus the wavelength scaling of the cutoff energy for the overall HHG is the same as that for the intraband HHG, i.e., wavelength independent.

Figure 4(b) shows the overall harmonic spectra calculated with wavelength 40.00 μm, 50.00 μm and 60.00 μm, respectively. One can see that the cutoff energies of the overall HHG are always near the 1.50 eV as indicated by the dashed pink line. Figure 4(c) shows the overall harmonic spectra with the laser wavelength varying from 40.00 μm to 60.00 μm in step of 2.50 μm. It is also found that the cutoff energies of the overall HHG are almost invariable and are fixed at 1.5 eV for the all wavelengths. Our results conform the fact that the cutoff energy of observed harmonics is independent of the laser wavelength when the intraband HHG is dominant in the cutoff region. This conclusion can also be verified very well by the harmonic spectra from the bulk silicon in the MIR regime shown in [34]. In this work, the low joint density of states (JDOS) leads to the suppression of the interband HHG within the cutoff region, i.e., the harmonics in the cutoff region are dominated by the intraband HHG in this model. This is the reason why authors concluded that the cutoff energy of observed harmonics is wavelength independent. The wavelength independence of the cutoff energy for the intraband HHG can also be understood by the rapid decreases of the orders of Bessel functions by expanding the intraband current into

Optics EXPRESS

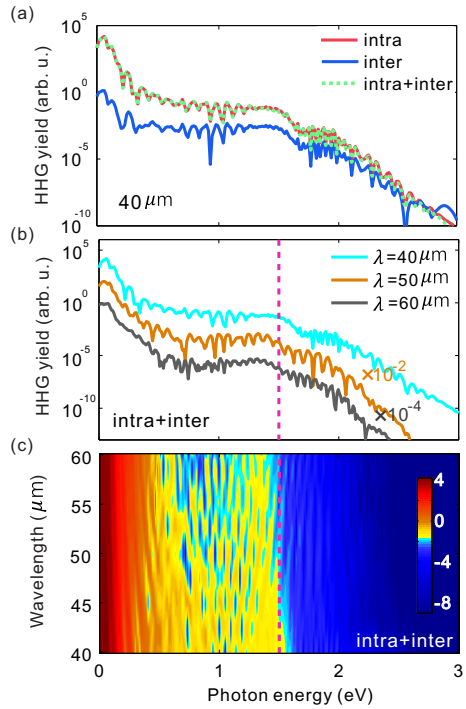

Fig. 4. (a) High harmonic spectra contributed by intraband, interband and overall currents with wavelength 40.00 μm. (b) High harmonic spectra contributed by overall currents with wavelength 40.00 μm, 50.00 μm and 60.00 μm. (c) High harmonic spectra (with a logarithmic color scale) contributed by overall currents with wavelength ranging from 40.00 μm to 60.00 μm. The vertical pink lines in panels (b) and (c) indicate the position of photon energy 1.50 eV. The laser intensity is 1.00×10^{10} W/cm^2 and the duration is 2 optical cycles for all laser pulses.

Bessel functions like the procedures in [6, 16].

The approach of separating intraband and interband contributions can be also used to explain the linear dependence of the cutoff energy on the field strength for the solid HHG. Figures 5(a) and 5(c) show the harmonic spectra contributed by the intraband and interband currents respectively for three field strengths (2.0×10^{-3} a.u., 4.5×10^{-3} a.u. and 7.0×10^{-3} a.u.) with a given wavelength 2.70 μm. The total duration of the laser pulse is 8 optical cycles. From the Figs. 5(a) and 5(c), one can see that the cutoff energies of both the intraband and interband HHG increase monotonously with the growing field strength as indicated by the pink and black arrows. The cutoff energies of the intraband and interband HHG as a function of the field strength F_0 are shown in Figs. 5(b) and 5(d), respectively. It is shown that the cutoff energies of both the intraband and interband HHG increase linearly with field strength F_0. Therefore, the cutoff energies of the observed harmonics always exhibit a linear dependence on the field strength, regardless of which mechanism is dominant. This is the reason why the linear dependence scaling on field strength is uncontroversial and is extensively accepted in research community.

4. Conclusion

In conclusion, we have theoretically studied the wavelength scaling of the cutoff energy for the solid HHG by decomposing the contributions into intraband and interband components. The cutoff energies of the intraband, interband and overall HHG are investigated respectively by

Optics EXPRESS

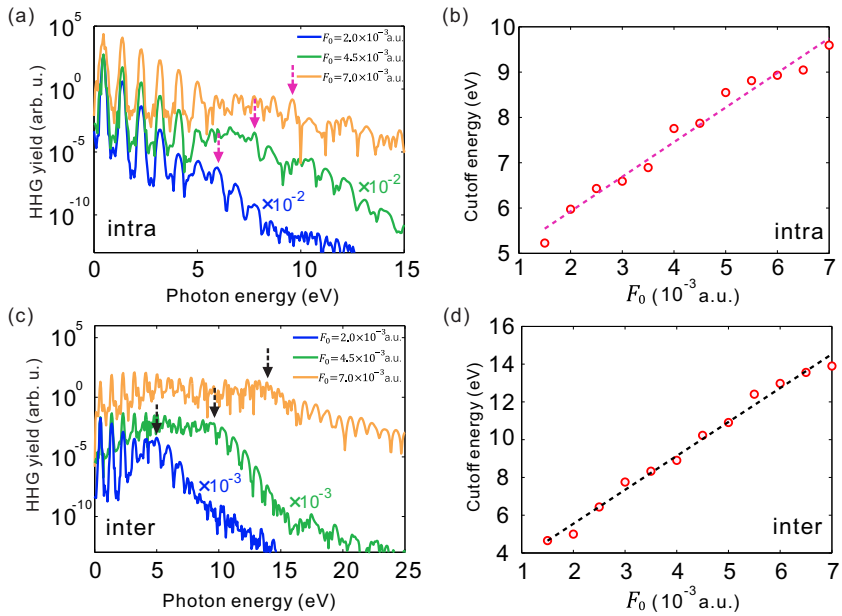

Fig. 5. High harmonic spectra contributed by the (a) intraband and (c) interband currents with the field strength 2.0×10^{-3} a.u., 4.5×10^{-3} a.u. and 7.0×10^{-3} a.u. The pink and black arrows indicate the cutoffs of the harmonic spectra. The cutoff energies of the (b) intraband and (d) interband HHG as a function of the field strength F_0. The laser wavelength is 2.70 μm and the duration is 8 optical cycles for all laser pulses.

varying the laser wavelength. Our simulations show that the cutoff energy of the intraband HHG is wavelength independent, whereas the cutoff energy of the interband HHG shows a linear dependence on laser wavelength. Our results reveal that two existing different wavelength scalings of the cutoff energy essentially stem from the fact that two different mechanisms may dominate the observed harmonics in the cutoff region. The widely accepted linear dependence of the cutoff energy on the field strength is also consistent with the interpretation involving the intraband and interband channels. Specifically, the cutoff energy of the observed harmonics always linearly depends on the field strength, because both of the intraband and interband HHG show a linear cutoff rule on the field strength. Our work clarifies the origin of two different wavelength scalings of the cutoff energy for the solid HHG. The significantly different wavelength dependences of the cutoff energy for intraband and interband HHG provide a promising way to distinguish the intraband and interband channels.

Funding

National Natural Science Foundation of China (NSFC) (11234004, 11404123, 11422435, 11627809, 11774109); Fundamental Research Funds for the Central Universities (2017KFXKJC002).

Acknowledgments

Numerical simulations presented in this paper were carried out using the High Performance Computing Center experimental testbed in SCTS/CGCL (see http://grid.hust.edu.cn/hpcc).